## CORONAVIRUS

# Effects of COVID-19 lockdowns on fine particulate matter concentrations

Melanie S. Hammer[1,2]*, Aaron van Donkelaar[2,1], Randall V. Martin[1,2], Erin E. McDuffie[1,2], Alexei Lyapustin[3], Andrew M. Sayer[3,4], N. Christina Hsu[3], Robert C. Levy[3], Michael J. Garay[5], Olga V. Kalashnikova[5], Ralph A. Kahn[3,6]

Lockdowns during the COVID-19 pandemic provide an unprecedented opportunity to examine the effects of human activity on air quality. The effects on fine particulate matter (PM$_{2.5}$) are of particular interest, as PM$_{2.5}$ is the leading environmental risk factor for mortality globally. We map global PM$_{2.5}$ concentrations for January to April 2020 with a focus on China, Europe, and North America using a combination of satellite data, simulation, and ground-based observations. We examine PM$_{2.5}$ concentrations during lockdown periods in 2020 compared to the same periods in 2018 to 2019. We find changes in population-weighted mean PM$_{2.5}$ concentrations during the lockdowns of −11 to −15 µg/m$^3$ across China, +1 to −2 µg/m$^3$ across Europe, and 0 to −2 µg/m$^3$ across North America. We explain these changes through a combination of meteorology and emission reductions, mostly due to transportation. This work demonstrates regional differences in the sensitivity of PM$_{2.5}$ to emission sources.

## INTRODUCTION

The onset of the coronavirus disease 2019 (COVID-19) pandemic resulted in unprecedented restrictions beginning in early 2020 in the form of economic shutdowns and limitations on mobility, in many places for extended periods of time. These unique conditions offer a rare opportunity to examine the effects of changes in human activity on air quality. Satellite images released early in the pandemic showed marked decreases in tropospheric nitrogen dioxide (NO$_2$), particularly over China. For example, a 48% reduction in NO$_2$ columns was observed over China in the 20 days after the Lunar New year compared to the 20 days prior (1). Anthropogenic NO$_2$ sources are mainly combustion processes, with power plant and transportation emissions being major sources (2–4). Of interest is how the COVID-19 restrictions affected ambient fine particulate matter (PM$_{2.5}$) concentrations, which are ranked as the leading environmental risk factor for mortality as part of the Global Burden of Disease (5).

PM$_{2.5}$ estimates are of particular relevance given the emerging evidence that exposure to PM$_{2.5}$ exacerbates the severity of COVID-19 infection systems and may increase the risk of death in patients with COVID-19 (6, 7). However, the accuracy of epidemiological studies of these associations depends on the availability and accuracy of ambient PM$_{2.5}$ data. Analysis of satellite observations is needed to supplement ground-based air quality monitoring networks that have limited spatial coverage and density in populated regions to better understand associations with health outcomes to inform decision-making activities (8).

PM$_{2.5}$ is formed from a variety of sources, both anthropogenic and natural. Anthropogenic sources of PM$_{2.5}$ include emissions from power plants and industrial activity, residential combustion, transportation, and agriculture. Natural sources include processes such as mineral dust, emission of biogenic volatile organic compounds (VOCs) from vegetation, wildfire smoke, and sea spray. These emissions can be either primary or secondary sources of PM$_{2.5}$. Primary sources directly emit particles to the atmosphere. Primary components of PM$_{2.5}$ include black carbon, primary organic aerosols, desert dust, and sea salt. The concentrations of these primary particles are considered to be generally linearly related to their emissions. However, the relationship between secondary sources and PM$_{2.5}$ concentrations is much more complicated and can be highly nonlinear (9). Secondary components of PM$_{2.5}$ include secondary inorganic and organic aerosols. Secondary inorganic aerosols include the sulfate-nitrate-ammonium system of aerosols, which are formed through the gas-to-particle conversion of sulfur dioxide (SO$_2$), nitrogen oxides (NO$_x$ = NO + NO$_2$), and ammonia (NH$_3$) gases. This system, in particular, can be highly nonlinear in terms of the relationship between emissions and aerosol formation (10, 11). Secondary organic aerosols are formed through the partitioning of oxidized VOCs to particles in the atmosphere. This system can also be highly sensitive to nonlinearities in the relationship between emissions of gases such as NO$_x$ and organic aerosol formation (12–14). Therefore, a substantial reduction in NO$_x$ emissions may not necessarily result in a substantial reduction in total PM$_{2.5}$ mass.

In line with a nonlinear chemical response, initial studies examining the effects of the COVID-19 lockdowns on PM$_{2.5}$ concentrations using ground monitor data and chemical transport modeling have found somewhat unexpected results. Several studies showed that even with the strict restrictions put in place in China, there were several severe haze episodes, particularly over northern China. These episodes were found to be caused by a combination of stagnant meteorological conditions and increased secondary aerosol formation from power plant emissions coupled with an increased atmospheric oxidation capacity, despite substantial reductions in transportation emissions and manufacturing (15–20). Initial studies examining air pollution over the United States and Europe found that, although there were mostly substantial decreases in NO$_x$ concentrations, there were little to no decreases in PM$_{2.5}$ concentrations

[1]Department of Energy, Environmental, and Chemical Engineering, Washington University in St. Louis, St. Louis, MO 63130, USA. [2]Department of Physics and Atmospheric Science, Dalhousie University, Halifax, NS, Canada. [3]Earth Sciences Division, NASA Goddard Space Flight Center, Greenbelt, MD 20771, USA. [4]Goddard Earth Sciences Technology and Research, Universities Space Research Association, Greenbelt, MD 21046, USA. [5]Jet Propulsion Laboratory, California Institute of Technology, Pasadena, CA 91109, USA. [6]Department of Atmospheric and Oceanic Science, University of Maryland, College Park, MD 20742, USA.
*Corresponding author. Email: melanie.hammer@wustl.edu

(21–28). These initial insights into the PM$_{2.5}$ system based on sparse monitoring motivate a more comprehensive assessment that includes satellite aerosol observations.

Recent advances in satellite remote sensing offer increasingly precise and accurate information (29–32). Using methods developed over the past decade (33–36), we map global PM$_{2.5}$ concentrations inferred using aerosol optical depth (AOD) from several satellite instruments, which are combined and related to PM$_{2.5}$ concentrations using relationships between surface PM$_{2.5}$ and total column AOD simulated with a chemical transport model (GEOS-Chem). Geographically weighted regression (GWR) is applied to predict and account for the residual bias with regional ground monitor data over China, Europe, and North America, areas with considerable ground monitor density, producing regional monthly mean estimates

for January to April 2018, 2019, and 2020 (Materials and Methods). We focus our analysis on these regions to compare PM$_{2.5}$ concentrations during the lockdown months in 2020 to the same time period in the previous 2 years (2018 and 2019) to assess the effects of restrictions on PM$_{2.5}$ levels. Using sensitivity simulations conducted with the GEOS-Chem model, we examine the impacts on PM$_{2.5}$ concentrations of possible emission reductions during the pandemic, particularly in the transportation sector, and assess the possible influence of natural variability in meteorology.

## RESULTS

Our global satellite-derived PM$_{2.5}$ estimates during the onset of the COVID-19 pandemic in January to April 2020 are described in



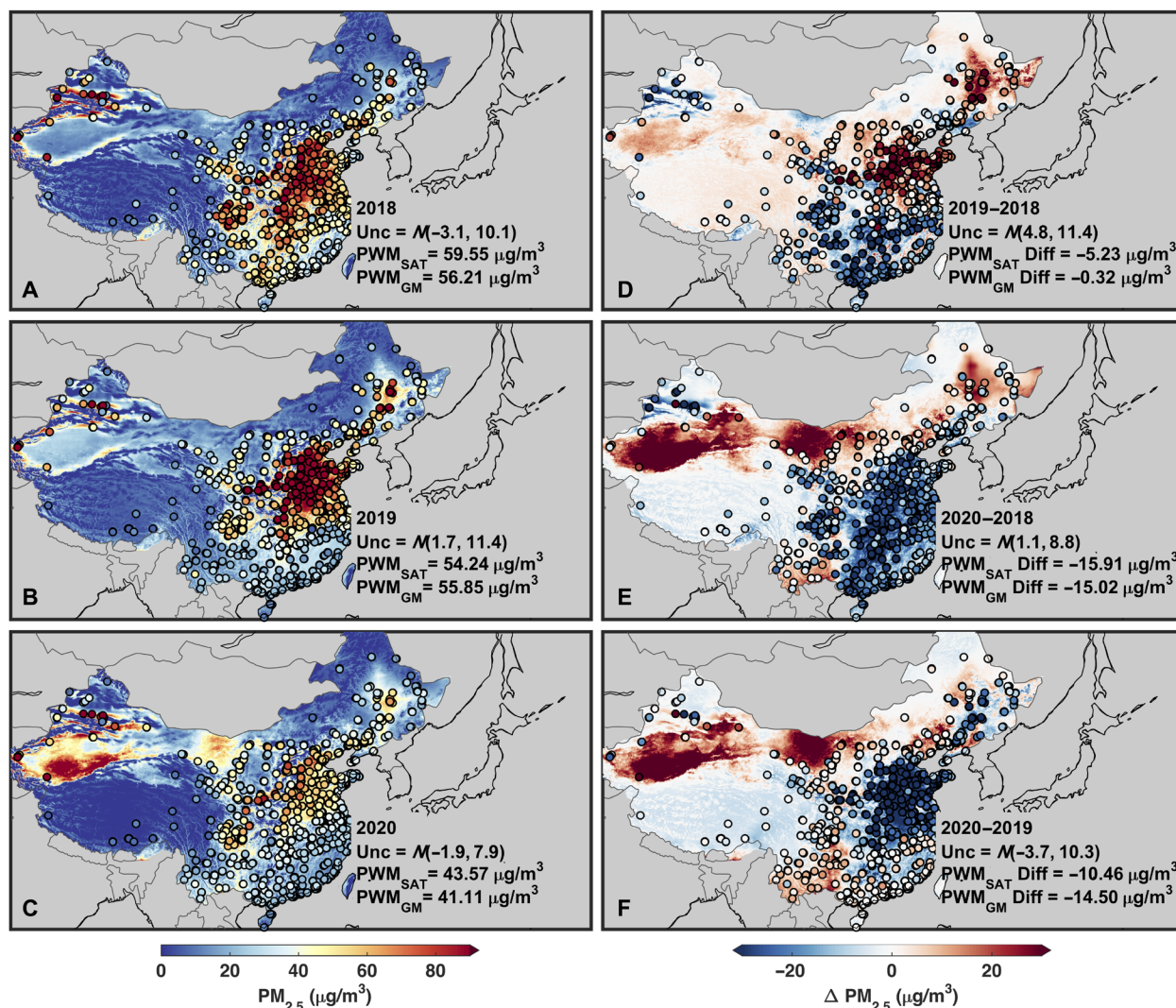**Fig. 1. Monthly mean PM$_{2.5}$ concentrations over China for February.** The three panels to the left show the monthly mean satellite-derived PM$_{2.5}$ concentrations over China for February 2018 (**A**), 2019 (**B**), and 2020 (**C**), with corresponding ground monitor PM$_{2.5}$ concentrations overlaid in filled circles. Inset values show the normal distribution of uncertainty [$N$(bias, variance)] between collocated satellite and ground monitor PM$_{2.5}$ concentrations, the population-weighted mean satellite-derived PM$_{2.5}$ concentration collocated with ground monitor locations (PWM$_{SAT}$), and the population-weighted mean ground monitor PM$_{2.5}$ concentration (PWM$_{GM}$). The three panels to the right show the 2019 to 2018 (**D**), 2020 to 2018 (**E**), and 2020 to 2019 (**F**) differences in February mean satellite-derived PM$_{2.5}$ concentrations with the differences in ground monitor concentrations overlaid in filled circles. Inset values show the normal distribution of uncertainty [$N$(bias, variance)] between the collocated differences in satellite-derived PM$_{2.5}$ concentrations and the differences in ground monitor PM$_{2.5}$ concentrations, the population-weighted mean difference in satellite-derived PM$_{2.5}$ values (PWM$_{SAT}$ Diff) collocated to ground monitor locations, and the population-weighted mean difference in ground monitor PM$_{2.5}$ concentrations (PWM$_{GM}$ Diff).
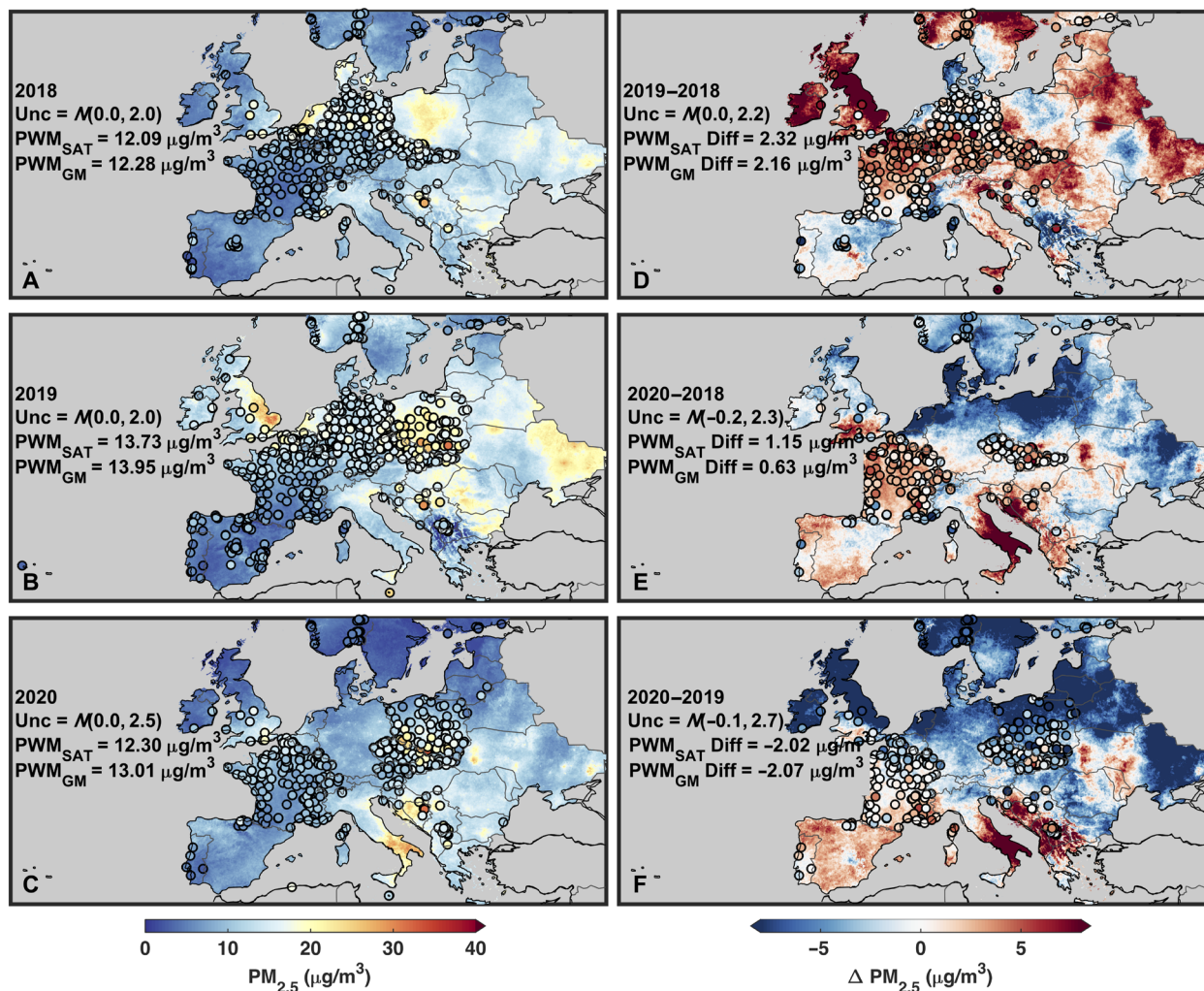
**Fig. 2. Monthly mean PM$_{2.5}$ concentrations over Europe for April.** Same as Fig. 1 but for April mean values over Europe. (**A**), (**B**), and (**C**) show the monthly mean satellite-derived PM$_{2.5}$ concentrations for April 2018, 2019, and 2020, respectively, with corresponding ground monitor PM$_{2.5}$ concentrations overlaid in filled circles. The three panels to the right show the 2019–2018 (**D**), 2020–2018 (**E**), and 2020–2019 (**F**) differences in April mean satellite-derived PM$_{2.5}$ concentrations with the differences in ground monitor concentrations overlaid in filled circles.

Materials and Methods and are shown in fig. S1. Ambient concentrations vary by more than an order of magnitude, reflecting a complex mixture of anthropogenic and natural sources, modulated by photochemical processing, atmospheric transport, and depositional loss. Below, we examine changes versus prior years for China, Europe, and North America where strict lockdowns occurred. Multiple lines of evidence indicate that the months with the largest emission reductions were February for China (37–40) and April for Europe and North America (37, 41–43). We treat these time periods as regional lockdown months. The months of January for China and January to February for Europe and North America are treated as nonlockdown control months.

The three left panels of Fig. 1 show the February mean satellite-derived PM$_{2.5}$ concentrations for 2018 (Fig. 1A), 2019 (Fig. 1B), and 2020 (Fig. 1C) over China with available PM$_{2.5}$ ground monitor concentrations overlaid in filled circles. The satellite-derived PM$_{2.5}$ and ground monitor concentrations are overall consistent (population-weighted bias < 2 µg/m$^3$, variance of 7.9 to 11.4 µg/m$^3$). The spatial

patterns between February 2018, 2019, and 2020 are similar, except for regions of northwest and north-central China exhibiting increases in PM$_{2.5}$ concentrations in 2020 of approximately 25 µg/m$^3$ and the North China Plain that exhibits a noticeable decrease in PM$_{2.5}$ concentrations in 2020 (concentrations between 45 and 55 µg/m$^3$) compared to the previous 2 years (concentrations between 65 and 80 µg/m$^3$). The increases over northwest and north-central China are in close proximity to the Taklamakan and Gobi deserts that induce variability in desert dust as indicated by prior studies (44–48) and by our GEOS-Chem simulations discussed below. The decrease over the densely populated North China Plain is somewhat reflected in the overall population-weighted mean values with reductions of 11 to 15 µg/m$^3$ in 2020 versus either 2018 or 2019. The difference plots (the three right panels of Fig. 1) reveal that this region shows increases of 10 to 15 µg/m$^3$ between 2019 and 2018 (Fig. 1D) and then switches to substantial decreases of −25 to −20 µg/m$^3$ for 2020 to 2018 (Fig. 1E) and −30 to −25 µg/m$^3$ for 2020 to 2019 (Fig. 1F). The stronger decreases visible between 2020 and 2019 compared to
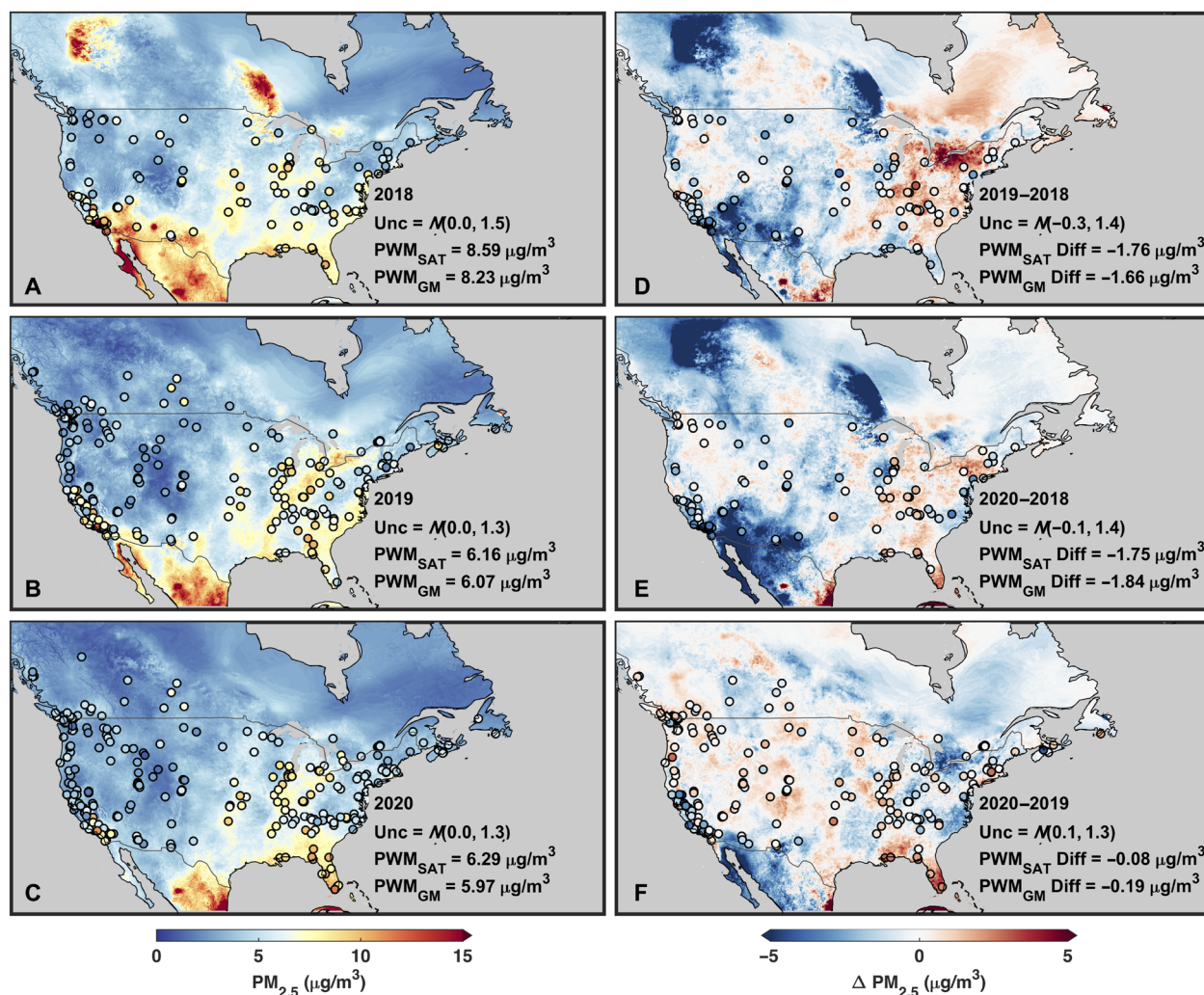
**Fig. 3. Monthly mean PM$_{2.5}$ concentrations over North America for April.** Same as Fig. 1 but for April mean values over North America. (**A**), (**B**), and (**C**) show the monthly mean satellite-derived PM$_{2.5}$ concentrations for April 2018, 2019, and 2020, respectively, with corresponding ground monitor PM$_{2.5}$ concentrations overlaid in filled circles. The three panels to the right show the 2019–2018 (**D**), 2020–2018 (**E**), and 2020–2019 (**F**) differences in April mean satellite-derived PM$_{2.5}$ concentrations with the differences in ground monitor concentrations overlaid in filled circles.

2020 and 2018 suggest some influence of natural variability. Examination of the nonlockdown month of January (fig. S2) reveals increases of +20 to +30 μg/m$^3$ over parts of this region for the 2019 to 2018, 2020 to 2018, and 2020 to 2019 differences. These results suggest substantial decreases in PM$_{2.5}$ concentrations in the North China Plain during the lockdown. Figure S3 shows a bar chart of population-weighted mean PM$_{2.5}$ concentrations over the North China Plain for both the satellite-derived and the ground monitor concentrations for all 3 years during the lockdown period (February) and outside the lockdown period (January). The concentrations for January are higher for all 3 years (population-weighted mean between 80 and ~100 μg/m$^3$) than during February with a small increase between 2019 and 2020. However, February shows a substantial decrease from ~70 μg/m$^3$ in 2018 and 2019 to ~50 μg/m$^3$ in 2020.

For the lockdown month of April over Europe (Fig. 2), the satellite-derived concentrations and ground-based measurements are again consistent (population-weighted bias within 0.1 μg/m$^3$), with both datasets exhibiting lower PM$_{2.5}$ concentrations in western

than eastern Europe. COVID-19–related changes are not immediately obvious when comparing the April 2020 values with the April 2018 and 2019 values, except for weak signals near Benelux. Interannual differences in PM$_{2.5}$ concentrations exhibit both positive and negative anomalies that depend strongly on reference year. Examination of the nonlockdown months of January to February (fig. S4) reveals even larger interannual differences than during the lockdown months.

For April over North America (Fig. 3), the satellite-derived and ground monitor concentrations are again consistent (population-weighted bias < 0.1 μg/m$^3$). Interannual variability is again dependent on comparison years, with the smallest population-weighted mean differences between April 2020 and 2019, which are comparable to the bias in the estimates versus ground monitors. Overall, the interannual variability of PM$_{2.5}$ concentrations and their population-weighted mean values during the lockdown are similar to the interannual variability and population-weighted mean values for the nonlockdown months (January to February 2020; fig. S5).
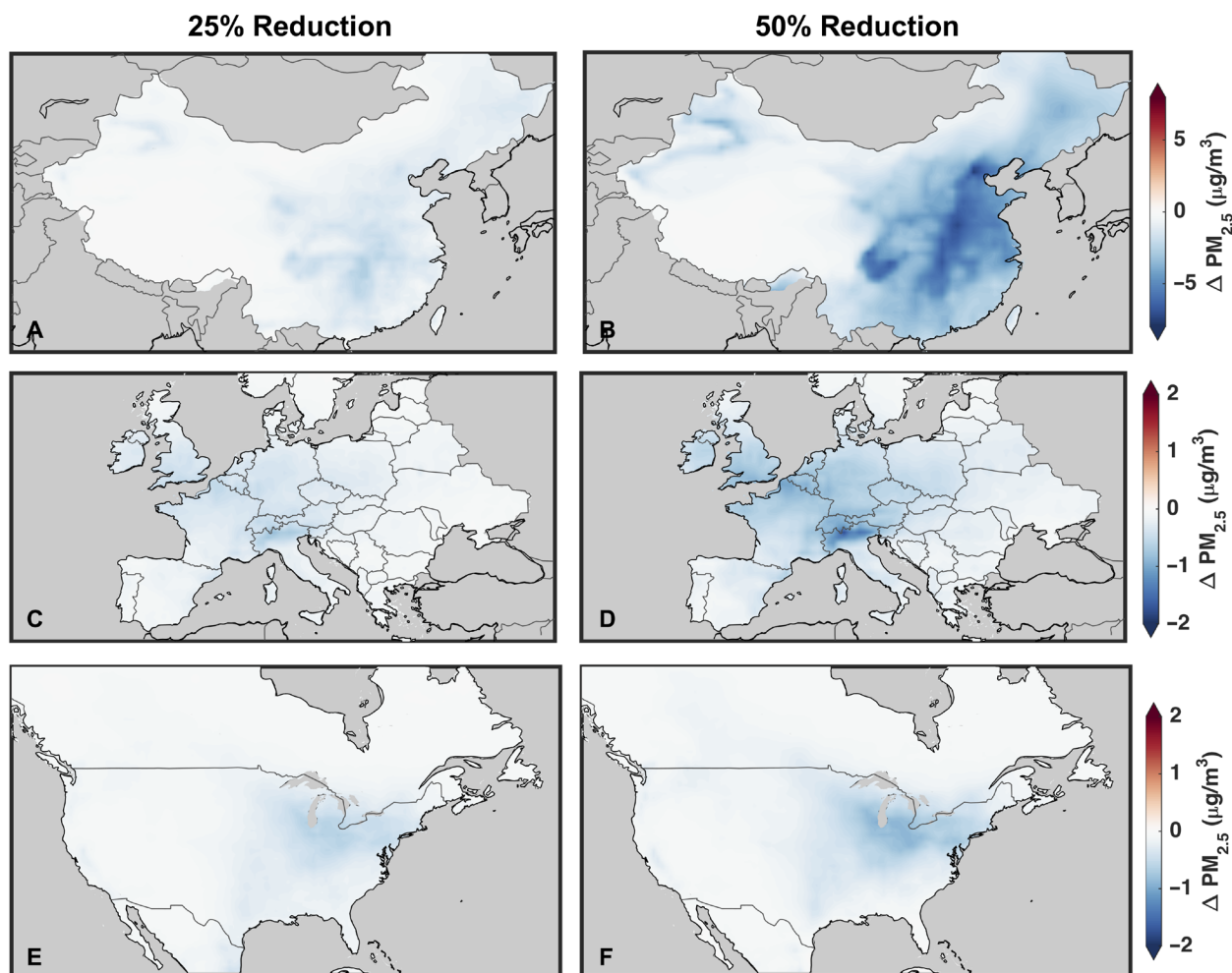
**Fig. 4. Change in simulated PM$_{2.5}$ due to transportation emission reductions.** Change in simulated surface PM$_{2.5}$ concentrations due to a 25% (left column) and 50% (right column) reduction in transportation emissions of all species for February 2020 over China (**A** and **B**), April 2020 over Europe (**C** and **D**), and April 2020 over North America (**E** and **F**).

To investigate how changes in emissions during the lockdown periods contribute to the changes (or lack of) in PM$_{2.5}$ concentrations, we conduct sensitivity simulations using the GEOS-Chem model with reduced transportation emissions and reduced NO$_x$ emissions across all anthropogenic sources (see Materials and Methods). The spatial pattern and extent of transportation reductions in 2020 are not well known, but reported reductions in fuel consumption (*37*, *43*, *49*) and observed NO$_2$ columns (*41*, *42*, *50*) suggest regional transportation reductions ranging from 25 to 50% with larger local reductions in specific urban areas. Therefore, we conduct two test cases with commensurate emission reductions.

Figure 4 shows the change in simulated PM$_{2.5}$ due to 25 and 50% reductions in transportation emissions, whereas fig. S6 shows the change in simulated PM$_{2.5}$ due to 25 and 50% reductions in anthropogenic NO$_x$ emissions. Decreases in PM$_{2.5}$ occur primarily near major urban and industrial regions in all scenarios, reflecting the distribution of transportation and industrial emissions modulated by atmospheric chemistry. Some simulated PM$_{2.5}$ decreases such as over the North China Plain and central Europe align with observed changes (Figs. 1 to 3); however, emission reductions cannot explain most of the observed changes in either magnitude or distribution.

Examination of changes in simulated PM$_{2.5}$ chemical composition offers insight into the magnitude of the effects. Reductions in all three regions are driven by reductions in nitrate aerosol due to reduced NO$_x$ emissions in all scenarios (figs. S7 and S8). These nitrate reductions are partially compensated by increases in sulfate and changes in ammonium, reflecting feedbacks on sulfur oxidation, aerosol thermodynamics, and heterogeneous chemistry. Similar feedbacks have been found in other sensitivity simulations to changes in NO$_x$ emissions (*15*, *51*). Feedbacks on the secondary organic aerosol system may also play a role due to changes in oxidants (*18*, *52*) and to aerosol acidity (*53*, *54*). The response found here highlights the nonlinearity between emission changes, the sulfate-nitrate-ammonium system, and PM$_{2.5}$ formation processes (*55*, *56*).

Ambient PM$_{2.5}$ concentrations are strongly influenced by meteorological conditions (*57–59*) that alter natural emissions, photochemical production, advection, and depositional loss. Therefore, we examine how natural variability due to meteorology coupled with reductions in emissions affects PM$_{2.5}$. The left column of Fig. 5 shows results from a GEOS-Chem sensitivity simulation where the change in PM$_{2.5}$ between 2020 and 2019 during the lockdown months

**Meteorology**

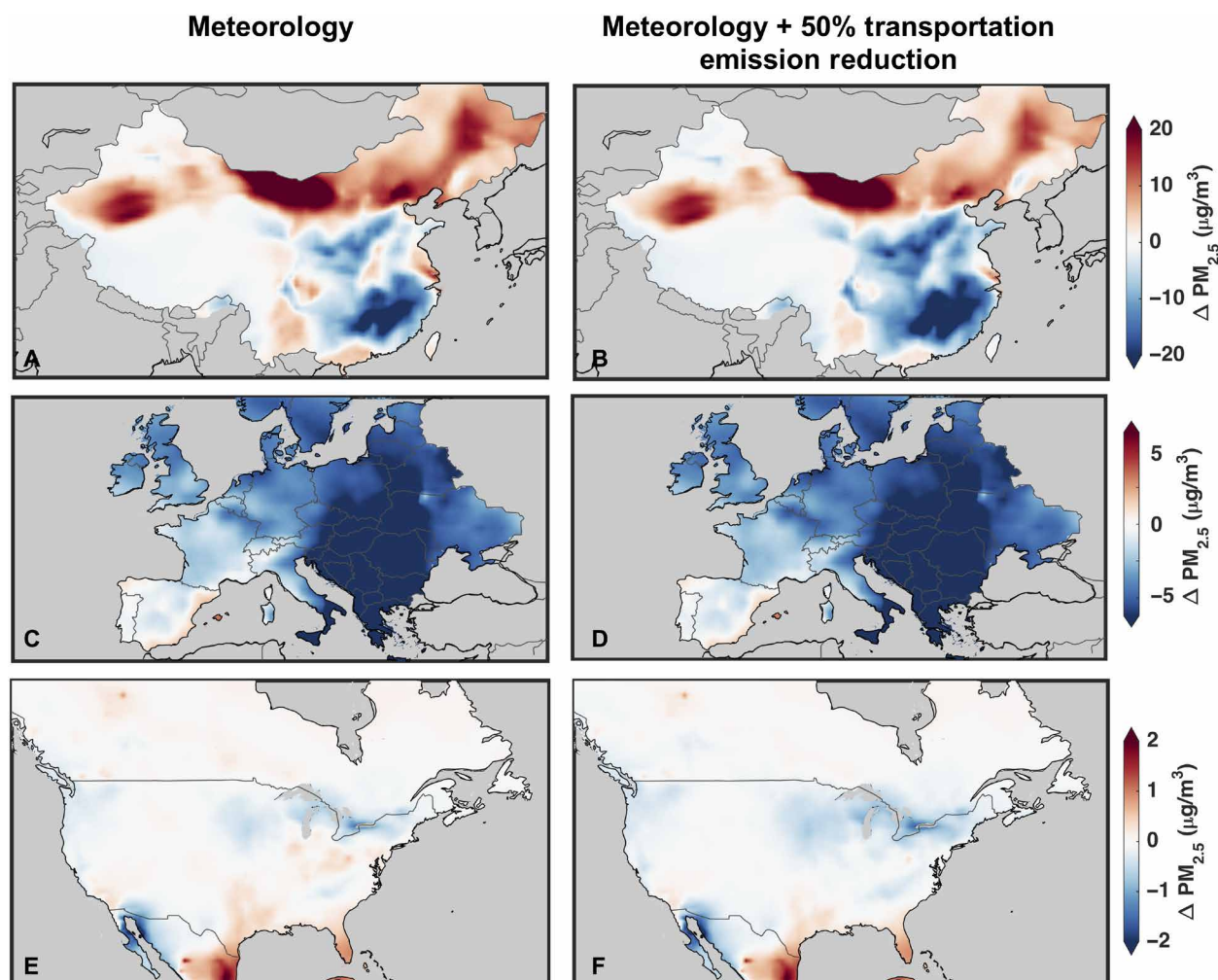**Meteorology + 50% transportation emission reduction**



**Fig. 5. Change in simulated PM$_{2.5}$ during the lockdown periods due to meteorology and emissions.** The 2020 to 2019 difference in simulated surface PM$_{2.5}$ concentrations due to meteorology (with emissions held constant; left column) and due to meteorology combined with a 50% reduction in transportation emissions (right column) for February over China (**A** and **B**), April over Europe (**C** and **D**), and April over North America (**E** and **F**).

is due solely to changes in meteorology, leaving emissions constant. The right column shows the change in PM$_{2.5}$ between 2020 and 2019 during the lockdown months due to meteorology and a 50% reduction in transportation emissions. Meteorology has major influences as discussed in the Supplementary Materials (Supplementary Text). Over China, much of the spatial pattern in PM$_{2.5}$ concentration differences seen in Fig. 1 can be explained by natural variability (Fig. 5A), except for a region showing decreases of <−20 μg/m$^3$ toward southern China that is weaker in the satellite-derived estimates. Meteorology alone is insufficient to explain the reductions in the North China Plain; there is a mixture of increases and decreases up to ±10 μg/m$^3$. When including the 50% transportation emission reductions (Fig. 5B), the small increases disappear, and decreases as low as −20 μg/m$^3$ near the North China Plain develop, similar to the observed decreases in satellite-derived PM$_{2.5}$ over the region. This suggests that the decreases observed over this region during the lockdown are driven by a combination of meteorology and emission reductions. In southern China, the overestimated reductions versus observations likely, in part, reflect within-country variation in the extent of emission reductions with the lockdown focus

further to the north. Meteorological variability largely explains the observations of increases of approximately 25 μg/m$^3$ in PM$_{2.5}$ over northwest and north-central China, supporting that they are driven by natural variability in desert dust. Most of eastern and northern Europe shows decreases between −2 and −8 μg/m$^3$ due to natural variability (Fig. 5C), which is comparable to the PM$_{2.5}$ estimates in Fig. 2. One possible exception is the Benelux region that has weak changes due to meteorology but displays decreases in the PM$_{2.5}$ estimates (Fig. 2). The combination of meteorology and reduced transportation emissions provides suggestive evidence of a regional COVID signal on top of larger natural variability. Over North America, meteorology appears to largely explain the small PM$_{2.5}$ changes between 2019 and 2020, but there is some evidence that transportation emission reductions contribute to the strength of the observed reduction in the Great Lakes region (Fig. 3).

**DISCUSSION**

The role of PM$_{2.5}$ as the leading global environmental risk factor for mortality, coupled with emerging evidence of the association of

ambient $PM_{2.5}$ with COVID-19 outcomes, motivates attention to assessing ambient $PM_{2.5}$ concentrations during the COVID-19 pandemic and understanding how societal interventions in response to the pandemic modulated ambient concentrations. Estimates of ambient concentrations during the pandemic are needed for epidemiological studies designed to better understand the relationship between COVID-19 and $PM_{2.5}$ concentrations. However, gaps in ground-based monitoring, coupled with latency in availability of monitoring data, motivate alternative measures of $PM_{2.5}$ from satellite remote sensing as inferred here. This activity builds upon a suite of advances across the satellite remote sensing community over the past decade with increasingly accurate and precise information at increasingly fine resolution. These satellite-derived $PM_{2.5}$ concentrations offer timely information about air quality evolution during the COVID-19 pandemic.

Despite the widely reported pronounced reductions in ambient $NO_2$ concentrations during COVID-19 lockdowns, we find that evidence of $PM_{2.5}$ reductions specifically associated with COVID-19 lockdowns requires greater attention to discern, reflecting the complexity of $PM_{2.5}$ sources and processes. The satellite-derived $PM_{2.5}$ concentrations inferred here offer timely information in regions lacking public monitor data, whereas the addition of simulation and ground monitor data offers multiple constraints on the $PM_{2.5}$ system. Comparison of $PM_{2.5}$ during the lockdown months in 2020 to the same time period in the previous 2 years (2018 and 2019) reveals interannual variability that depends strongly on the reference year, implying a dominant meteorological influence in most regions. We find changes in population-weighted mean $PM_{2.5}$ concentrations during COVID-19 lockdowns of $-11$ to $-15$ $\mu g/m^3$ for China, $-2$ to $+1$ $\mu g/m^3$ for Europe, and $0$ to $-2$ $\mu g/m^3$ for North America. Detection of changes in $PM_{2.5}$ over North America and Europe may be complicated by the lower background levels in these regions, rendering the relative reductions difficult to discern. GEOS-Chem simulations provide supporting evidence of the combined influence of meteorology and emission reductions on features discernible during the COVID-19 lockdowns, particularly over the North China Plain with weaker signals over Benelux and the Great Lakes regions. The response of $PM_{2.5}$ to COVID-19 lockdowns offers insight into the sensitivity of $PM_{2.5}$ to transportation and other sources affected by the lockdowns. The strongest COVID-19 signal is a reduction of about 5 to 10 $\mu g/m^3$ over the North China Plain during February, followed by reductions of a few micrograms per cubic meter during April near the Benelux region of northern Europe, followed by suggestive evidence of reductions of less than 1 $\mu g/m^3$ in the Great Lakes region. Natural meteorological variability dominates elsewhere.

Long-term trends in emission reductions may also contribute to the $PM_{2.5}$ reductions found here. Satellite-derived $PM_{2.5}$ data indicate recent trends before COVID-19 of about $-3.7$ $\mu g/m^3$ per year for China, $-0.15$ $\mu g/m^3$ per year for Europe, and $-0.28$ $\mu g/m^3$ per year for the eastern United States (33). These "business-as-usual" trends driven by emission controls are generally weaker than the observed anomalies during COVID-19 lockdowns but are nonetheless large enough to be a contributing factor.

This work demonstrates the complex relationship between secondary emission sources and $PM_{2.5}$ concentrations; reductions in $NO_x$ emissions over all three regions are partially offset by nonlinearities in atmospheric chemistry. The weak sensitivity of $PM_{2.5}$ to emissions from transportation is consistent with prior work. At the global scale, the transportation sector has been estimated to contribute 5 to 12% of population-weighted $PM_{2.5}$ (60–62). At the regional

scale, the contribution of the transportation sector to total $PM_{2.5}$ has been estimated to be approximately 17% for China (63), approximately 14% for Europe (64), and less than 10% over the United States (65, 66). Rather, the more dominant sources of $PM_{2.5}$ from biofuel and mineral dust (60–62) were unlikely to have been strongly affected by the COVID-19 lockdowns. Future advances in quantifying emission changes associated with COVID-19 lockdowns will enable more precise estimates of the sensitivity of $PM_{2.5}$ to its sources.

## MATERIALS AND METHODS

### Satellite AOD sources

Satellite AOD from six retrieval products from three satellite instruments is used to infer ambient $PM_{2.5}$ concentrations. Twin Moderate Resolution Imaging Spectroradiometer (MODIS) instruments on the Terra and Aqua satellites provide daily global coverage. The Multiangle Imaging Spectroradiometer (MISR) instrument, which is also on the Terra satellite, provides global coverage about once per week.

The Dark Target (DT) algorithm (29) processes collection 6.1 MODIS radiances from both the Terra and Aqua satellites individually and is designed to retrieve AOD over dark surfaces (e.g., vegetated land surfaces and dark soils) by performing a simultaneous inversion of two visible (470 and 660 nm) and one shortwave-infrared (2120 nm) channel. The DT algorithm retrieves AOD at 550 nm at a spatial resolution of 10 km.

The Deep Blue (DB) algorithm (30) also processes collection 6.1 MODIS radiances from both Terra and Aqua individually and uses blue wavelength measurements where the surface reflectance over land tends to be much lower than at longer wavelengths, allowing for the retrieval of aerosol properties over both bright and dark surfaces. This is especially true over desert surfaces. The DB algorithm retrieves AOD at 550 nm at a spatial resolution of 10 km.

The Multiangle Implementation of Atmospheric Correction (MAIAC) algorithm (31) uses a dynamic minimum reflectance method to characterize spectral surface reflectance ratios by jointly processing MODIS radiances from the Terra and Aqua satellites. The MAIAC algorithm retrieves AOD at 466 nm over both bright and dark land surfaces including deserts. MAIAC reports AOD daily for MODIS Terra and Aqua observations at 466 and 550 nm at a fine spatial resolution of 1 km.

The MISR v23 algorithm (32) retrieves AOD from radiances measured by the MISR instrument, which observes Earth at nine different viewing angles and four spectral bands (446, 558, 672, and 866 nm), with a swath width of 380 km at all view angles that provides global coverage about once per week, every 9 days at the equator, and up to every 2 days near the poles. The MISR retrieval algorithm uses the same-scene multiangular views provided by the nine view angles to solve for surface and top-of-atmosphere reflectance contributions, providing AOD retrievals over bright and dark land surfaces without absolute surface reflectance assumptions. The MISR v23 algorithm retrieves AOD at 550 nm at a spatial resolution of 4.4 km.

### Ground monitor data

We use ground monitor data over North America and Europe from Open AQ (https://openaq.org/) for timely total $PM_{2.5}$ mass information. To help promote data quality, we only use data from government monitoring sites. Over China, we use data collected by the Chinese government (http://beijingair.sinaapp.com/). Daily

observations at each site are aggregated to monthly means, and sites with greater than 10 observations per month were included.

## GEOS-Chem simulations

We use the GEOS-Chem chemical transport model (67) v11-01 simulation described by Hammer *et al.* (33) as a data source for AOD and to represent the relationship of surface $PM_{2.5}$ to total column AOD. The GEOS-Chem model solves for the evolution of atmospheric aerosols and gases using a detailed oxidant-aerosol chemical mechanism, emission inventories, and assimilated meteorological data. The assimilated meteorological data are from the Modern-Era Retrospective analysis for Research and Applications, Version 2 (MERRA-2) Reanalysis of the NASA Global Modeling and Assimilation Office (68). We conduct our simulation for January to April 2018 to 2020. We use the global spatial resolution of 2° × 2.5° and the nested spatial resolution of 0.5° × 0.625° over North America, Europe, and Asia with 47 vertical layers. The top of the lowest model layer is ~100 m. Regional anthropogenic emission inventories of aerosols and their precursors are used over the United States [EPA/NEI11 (69)], Europe (EMEP; www.emep.int), and China [MEIC (70)].

For our sensitivity simulations with reduced emissions from transportation and of $NO_x$, we used the above simulation but with the Community Emissions Data System emission inventory, updated for the Global Burden of Disease–Major Air Pollution Sources project (CEDS_GBD-MAPS) (2). This global gridded inventory includes detailed sectoral information and enables consistent sectoral perturbations across all world regions. The transportation sector includes both road transportation and off/nonroad transportation emissions. Simulations with reduced $NO_x$ emissions include reductions in NO emissions from all anthropogenic sectors included in the CEDS inventory (agriculture, energy, industry, road transportation, off/nonroad transportation, residential/commercial, solvents, and waste). These sensitivity simulations build upon emerging information about emission changes during COVID-19 interventions. The transportation sector appears to have had some of the largest reductions (49, 71), so we focus on that sector with reductions of 25 and 50%. The observed reductions in $NO_2$ columns (41, 50, 72) indicate emission reductions primarily from transportation but potentially from the power and industry sectors as well. Thus, we conduct additional sensitivity simulations with total $NO_x$ reductions of 25 and 50% across all sectors. We conduct simulations with reductions across entire regions, given knowledge gaps in the spatial distribution of emission reductions.

## Estimating $PM_{2.5}$ concentrations from satellite simulation and ground monitors

We first produce monthly geophysical-based estimates of surface $PM_{2.5}$ concentrations using a combination of satellites and simulation following Hammer *et al.* (33). We then statistically fuse these geophysical-based estimates with regional ground monitor data following van Donkelaar *et al.* (34) to obtain monthly regional geophysical-statistical hybrid $PM_{2.5}$ estimates for China, Europe, and North America.

To produce the geophysical-based $PM_{2.5}$ estimates, we combine AOD from several satellite products (MODIS DB, MODIS DT, MISR, and MAIAC) based on their relative uncertainties with the global sun photometer network AERONET (V3) (73), which provides AOD measurements with high accuracy (uncertainty < 0.02). Simulated AOD from GEOS-Chem is also used as an additional AOD

source; however, its contributions are mostly over northern regions where satellite retrievals are sparse (33). Satellite observations comprise 89% of the global combined population-weighted AOD data for the February to April 2018 to 2020 period (individual contributions to the global population-weighted mean: 22% MAIAC, 16% MODIS DB Terra and Aqua, 14% MODIS DT Terra and Aqua, and 7% MISR).

To estimate surface concentrations of $PM_{2.5}$ from satellite AOD, we use the local, coincident ratio of simulated surface $PM_{2.5}$ concentrations to simulated total column AOD. This ratio is a function of the factors that relate $PM_{2.5}$ mass to satellite observations of AOD (e.g., aerosol size, aerosol composition, diurnal variation, relative humidity, and the vertical structure of aerosol extinction) (74).

The inability to retrieve satellite AOD in the presence of snow or cloud cover introduces sampling limitations when calculating $PM_{2.5}$ from satellite AOD (75). We use GEOS-Chem to address these sampling limitations by scaling the satellite AOD by the ratio of simulated monthly mean AOD to simulated AOD coincident with satellite AOD. This approach builds upon the assimilated meteorology and mechanistic representation of processes such as photochemical feedbacks and deposition that are included in GEOS-Chem.

We then use GWR following van Donkelaar *et al.* (34) to predict the bias between the monthly geophysical-based $PM_{2.5}$ estimates and the regional ground monitor observations. The GWR is conducted at a 1-km resolution to calibrate monthly parameter coefficients based on comparison with coincident ground monitor observations. The bias predicted by the GWR is used to adjust the geophysical-based $PM_{2.5}$ mass estimate to produce the monthly geophysical-statistical hybrid $PM_{2.5}$ estimates. Figure S9 shows the resulting hybrid $PM_{2.5}$ estimates compared to ground monitor data for North America, Europe, and China for January to April 2018 to 2020.

## Population estimates

Population estimates are from the Gridded Population of the World (GPW v4) database (76). The 2018 and 2019 population estimates were obtained by linearly interpolating between 2015 and 2020. Population-weighted mean $PM_{2.5}$ values are calculated as a weighted average weighted by the population estimates for the same year.

## REFERENCES AND NOTES

1. F. Liu, A. Page, S. A. Strode, Y. Yoshida, S. Choi, B. Zheng, L. N. Lamsal, C. Li, N. A. Krotkov, H. Eskes, R. van der A, P. Veefkind, P. F. Levelt, O. P. Hauser, J. Joiner, Abrupt decline in tropospheric nitrogen dioxide over China after the outbreak of COVID-19. *Sci. Adv.* **6**, eabc2992 (2020).

2. E. McDuffie, S. Smith, P. O'Rourke, K. Tibrewal, C. Venkataraman, E. Marais, B. Zheng, M. Crippa, M. Brauer, R. Martin, CEDS_GBD-MAPS: Global anthropogenic emission inventory of $NO_x$, $SO_2$, CO, $NH_3$, NMVOCs, BC, and OC from 1970-2017 (2020).

3. R. M. Hoesly, S. J. Smith, L. Feng, Z. Klimont, G. Janssens-Maenhout, T. Pitkanen, J. J. Seibert, L. Vu, R. J. Andres, R. M. Bolt, T. C. Bond, L. Dawidowski, N. Kholod, J. Kurokawa, M. Li, L. Liu, Z. Lu, M. C. P. Moura, P. R. O'Rourke, Q. Zhang, Historical (1750–2014) anthropogenic emissions of reactive gases and aerosols from the Community Emissions Data System (CEDS). *Geosci. Model Dev.* **11**, 369–408 (2018).

4. M. Crippa, G. Janssens-Maenhout, F. Dentener, D. Guizzardi, K. Sindelarova, M. Muntean, R. Van Dingenen, C. Granier, Forty years of improvements in European air quality: Regional policy-industry interactions with global impacts. *Atmos. Chem. Phys.* **16**, 3825–3841 (2016).

5. GBD 2019 Risk Factors Collaborators, Global burden of 87 risk factors in 204 countries and territories, 1990–2019: A systematic analysis for the Global Burden of Disease Study 2019. *Lancet* **396**, 1223–1249 (2020).

6. E. Conticini, B. Frediani, D. Caro, Can atmospheric pollution be considered a co-factor in extremely high level of SARS-CoV-2 lethality in Northern Italy? *Environ. Pollut.* **261**, 114465 (2020).

7. X. Wu, R. C. Nethery, M. B. Sabath, D. Braun, F. Dominici, Air pollution and COVID-19 mortality in the United States: Strengths and limitations of an ecological regression analysis. *Sci. Adv.* **6**, eabd4049 (2020).

8. R. V. Martin, M. Brauer, A. van Donkelaar, G. Shaddick, U. Narain, S. Dey, No one knows which city has the highest concentration of fine particulate matter. *Atmos. Environ. X.* **3**, 100040 (2019).

9. J. H. Kroll, C. L. Heald, C. D. Cappa, D. K. Farmer, J. L. Fry, J. G. Murphy, A. L. Steiner, The complex chemical effects of COVID-19 shutdowns on air quality. *Nat. Chem.* **12**, 777–779 (2020).

10. P. J. Adams, J. H. Seinfeld, D. M. Koch, Global concentrations of tropospheric sulfate, nitrate, and ammonium aerosol simulated in a general circulation model. *J. Geophys. Res. Atmos.* **104**, 13791–13823 (1999).

11. H. O. T. Pye, H. Liao, S. Wu, L. J. Mickley, D. J. Jacob, D. K. Henze, J. H. Seinfeld, Effect of changes in climate and emissions on future sulfate-nitrate-ammonium aerosol levels in the United States. *J. Geophys. Res. Atmos.* **114**, D01205 (2009).

12. A. G. Carlton, H. O. T. Pye, K. R. Baker, C. J. Hennigan, Additional benefits of federal air-quality rules: Model estimates of controllable biogenic secondary organic aerosol. *Environ. Sci. Technol.* **52**, 9254–9265 (2018).

13. C. R. Hoyle, M. Boy, N. M. Donahue, J. L. Fry, M. Glasius, A. Guenther, A. G. Hallar, K. Huff Hartz, M. D. Petters, T. Petäjä, T. Rosenoern, A. P. Sullivan, A review of the anthropogenic influence on biogenic secondary organic aerosol. *Atmos. Chem. Phys.* **11**, 321–343 (2011).

14. K. Tsigaridis, M. Krol, F. J. Dentener, Y. Balkanski, J. Lathière, S. Metzger, D. A. Hauglustaine, M. Kanakidou, Change in global aerosol composition since preindustrial times. *Atmos. Chem. Phys.* **6**, 5143–5162 (2006).

15. T. Le, Y. Wang, L. Liu, J. Yang, Y. L. Yung, G. Li, J. H. Seinfeld, Unexpected air pollution with marked emission reductions during the COVID-19 outbreak in China. *Science* **369**, 702–706 (2020).

16. Y. Chang, R. Huang, X. Ge, X. Huang, J. Hu, Y. Duan, Z. Zou, X. Liu, M. F. Lehmann, Puzzling haze events in China during the coronavirus (COVID-19) shutdown. *Geophys. Res. Lett.* **47**, e2020GL088533 (2020).

17. Y. Sun, L. Lei, W. Zhou, C. Chen, Y. He, J. Sun, Z. Li, W. Xu, Q. Wang, D. Ji, P. Fu, Z. Wang, D. R. Worsnop, A chemical cocktail during the COVID-19 outbreak in Beijing, China: Insights from six-year aerosol particle composition measurements during the Chinese New Year holiday. *Sci. Total Environ.* **742**, 140739 (2020).

18. X. Huang, A. Ding, J. Gao, B. Zheng, D. Zhou, X. Qi, R. Tang, J. Wang, C. Ren, W. Nie, X. Chi, Z. Xu, L. Chen, Y. Li, F. Che, N. Pang, H. Wang, D. Tong, W. Qin, W. Cheng, W. Liu, Q. Fu, B. Liu, F. Chai, S. J. Davis, Q. Zhang, K. He, Enhanced secondary pollution offset reduction of primary emissions during COVID-19 lockdown in China. *Natl. Sci. Rev.* **8**, nwaa137 (2021).

19. M. Li, T. Wang, M. Xie, S. Li, B. Zhuang, Q. Fu, M. Zhao, H. Wu, J. Liu, E. Saikawa, K. Liao, Drivers for the poor air quality conditions in North China Plain during the COVID-19 outbreak. *Atmos. Environ.* **246**, 118103 (2020).

20. P. Wang, K. Chen, S. Zhu, P. Wang, H. Zhang, Severe air pollution events not avoided by reduced anthropogenic activities during COVID-19 outbreak. *Resour. Conserv. Recycl.* **158**, 104814 (2020).

21. J. M. Baldasano, COVID-19 lockdown effects on air quality by $NO_2$ in the cities of Barcelona and Madrid (Spain). *Sci. Total Environ.* **741**, 140353 (2020).

22. Á. Briz-Redón, C. Belenguer-Sapiña, Á. Serrano-Aroca, Changes in air pollution during COVID-19 lockdown in Spain: A multi-city study. *J. Environ. Sci.* **101**, 16–26 (2021).

23. G. Donzelli, L. Cioni, M. Cancellieri, A. Llopis Morales, M. Morales Suárez-Varela, The effect of the Covid-19 lockdown on air quality in three italian medium-sized cities. *Atmosphere* **11**, 1118 (2020).

24. R. Tanzer-Gruener, J. Li, S. R. Eilenberg, A. L. Robinson, A. A. Presto, Impacts of modifiable factors on ambient air pollution: A case study of COVID-19 shutdowns. *Environ. Sci. Technol. Lett.* **7**, 554–559 (2020).

25. L.-W. A. Chen, L.-C. Chien, Y. Li, G. Lin, Nonuniform impacts of COVID-19 lockdown on air quality over the United States. *Sci. Total Environ.* **745**, 141105 (2020).

26. S. Zangari, D. T. Hill, A. T. Charette, J. E. Mirowsky, Air quality changes in New York City during the COVID-19 pandemic. *Sci. Total Environ.* **742**, 140496 (2020).

27. M. D. Adams, Air pollution in Ontario, Canada during the COVID-19 state of emergency. *Sci. Total Environ.* **742**, 140516 (2020).

28. H. A. Parker, S. Hasheminassab, J. D. Crounse, C. M. Roehl, P. O. Wennberg, Impacts of traffic reductions associated with COVID-19 on Southern California air quality. *Geophys. Res. Lett.* **47**, e2020GL090164 (2020).

29. R. C. Levy, S. Mattoo, L. A. Munchak, L. A. Remer, A. M. Sayer, F. Patadia, N. C. Hsu, The Collection 6 MODIS aerosol products over land and ocean. *Atmos. Meas. Tech.* **6**, 2989–3034 (2013).

30. N. C. Hsu, J. Lee, A. M. Sayer, W. Kim, C. Bettenhausen, S.-C. Tsay, VIIRS deep blue aerosol products over land: Extending the EOS long-term aerosol data records. *J. Geophys. Res. Atmos.* **124**, 4026–4053 (2019).

31. A. Lyapustin, Y. Wang, S. Korkin, D. Huang, MODIS Collection 6 MAIAC algorithm. *Atmos. Meas. Tech.* **11**, 5741–5765 (2018).

32. M. J. Garay, M. L. Witek, R. A. Kahn, F. C. Seidel, J. A. Limbacher, M. A. Bull, D. J. Diner, E. G. Hansen, O. V. Kalashnikova, H. Lee, A. M. Nastan, Y. Yu, Introducing the 4.4km spatial resolution Multi-Angle Imaging SpectroRadiometer (MISR) aerosol product. *Atmos. Meas. Tech.* **13**, 593–628 (2020).

33. M. S. Hammer, A. van Donkelaar, C. Li, A. Lyapustin, A. M. Sayer, N. C. Hsu, R. C. Levy, M. J. Garay, O. V. Kalashnikova, R. A. Kahn, M. Brauer, J. S. Apte, D. K. Henze, L. Zhang, Q. Zhang, B. Ford, J. R. Pierce, R. V. Martin, Global estimates and long-term trends of fine particulate matter concentrations (1998–2018). *Environ. Sci. Technol.* **54**, 7879–7890 (2020).

34. A. van Donkelaar, R. V. Martin, C. Li, R. T. Burnett, Regional estimates of chemical composition of fine particulate matter using a combined geoscience-statistical method with information from satellites, models, and monitors. *Environ. Sci. Technol.* **53**, 2595–2611 (2019).

35. A. van Donkelaar, R. V. Martin, M. Brauer, R. Kahn, R. Levy, C. Verduzco, P. J. Villeneuve, Global estimates of ambient fine particulate matter concentrations from satellite-based aerosol optical depth: Development and application. *Environ. Health Perspect.* **118**, 847–855 (2010).

36. A. van Donkelaar, R. V. Martin, R. J. D. Spurr, R. T. Burnett, High-resolution satellite-derived $PM_{2.5}$ from optimal estimation and geographically weighted regression over North America. *Environ. Sci. Technol.* **49**, 10482–10491 (2015).

37. Z. Liu, P. Ciais, Z. Deng, R. Lei, S. J. Davis, S. Feng, B. Zheng, D. Cui, X. Dou, B. Zhu, R. Guo, P. Ke, T. Sun, C. Lu, P. He, Y. Wang, X. Yue, Y. Wang, Y. Lei, H. Zhou, Z. Cai, Y. Wu, R. Guo, T. Han, J. Xue, O. Boucher, E. Boucher, F. Chevallier, K. Tanaka, Y. Wei, H. Zhong, C. Kang, N. Zhang, B. Chen, F. Xi, M. Liu, F.-M. Bréon, Y. Lu, Q. Zhang, D. Guan, P. Gong, D. M. Kammen, K. He, H. J. Schellnhuber, Near-real-time monitoring of global $CO_2$ emissions reveals the effects of the COVID-19 pandemic. *Nat. Commun.* **11**, 5172 (2020).

38. B. Zheng, G. Geng, P. Ciais, S. J. Davis, R. V. Martin, J. Meng, N. Wu, F. Chevallier, G. Broquet, F. Boersma, R. van der A, J. Lin, D. Guan, Y. Lei, K. He, Q. Zhang, Satellite-based estimates of decline and rebound in China's $CO_2$ emissions during COVID-19 pandemic. *Sci. Adv.* **6**, eabd4998 (2020).

39. Y. Tohjima, P. K. Patra, Y. Niwa, H. Mukai, M. Sasakawa, T. Machida, Detection of fossil-fuel $CO_2$ plummet in China due to COVID-19 by observation at Hateruma. *Sci. Rep.* **10**, 18688 (2020).

40. B. Silver, X. He, S. R. Arnold, D. V. Spracklen, The impact of COVID-19 control measures on air quality in China. *Environ. Res. Lett.* **15**, 084021 (2020).

41. M. Guevara, O. Jorba, A. Soret, H. Petetin, D. Bowdalo, K. Serradell, C. Tena, H. Denier Van Der Gon, J. Kuenen, V.-H. Peuch, C. Pérez García-Pando, Time-resolved emission reductions for atmospheric chemistry modelling in Europe during the COVID-19 lockdowns (2020); https://doi.org/10.5194/acp-2020-686.

42. D. L. Goldberg, S. C. Anenberg, D. Griffin, C. A. McLinden, Z. Lu, D. G. Streets, Disentangling the impact of the COVID-19 lockdowns on urban $NO_2$ from natural variability. *Geophys. Res. Lett.* **47**, e2020GL089269 (2020).

43. S. Ou, X. He, W. Ji, W. Chen, L. Sui, Y. Gan, Z. Lu, Z. Lin, S. Deng, S. Przesmitzki, J. Bouchard, Machine learning model to project the impact of COVID-19 on US motor gasoline demand. *Nat. Energy* **5**, 666–673 (2020).

44. X. Querol, A. Tobías, N. Pérez, A. Karanasiou, F. Amato, M. Stafoggia, C. Pérez García-Pando, P. Ginoux, F. Forastiere, S. Gumy, P. Mudu, A. Alastuey, Monitoring the impact of desert dust outbreaks for air quality for health studies. *Environ. Int.* **130**, 104867 (2019).

45. X. Wang, H. Cheng, H. Che, J. Sun, H. Lu, M. Qiang, T. Hua, B. Zhu, H. Li, W. Ma, L. Lang, L. Jiao, D. Li, Modern dust aerosol availability in northwestern China. *Sci. Rep.* **7**, 8741 (2017).

46. A. L. Dement'eva, G. S. Zhamsueva, A. S. Zayakhanov, V. V. Tsydypov, A. A. Ayurzhanaev, D. Azzaaya, D. Oyunchimeg, Mass concentration of $PM_{10}$ and $PM_{2.5}$ fine-dispersed aerosol fractions in the Eastern Gobi desert. *Russ. Meteorol. Hydrol.* **38**, 80–87 (2013).

47. D. Rupakheti, X. Yin, M. Rupakheti, Q. Zhang, P. Li, M. Rai, S. Kang, Spatio-temporal characteristics of air pollutants over Xinjiang, northwestern China. *Environ. Pollut.* **268**, 115907 (2021).

48. J. Li, S. Wang, J. Chu, J. Wang, X. Li, M. Yue, K. Shang, Characteristics of air pollution events over Hotan Prefecture at the southwestern edge of Taklimakan Desert, China. *J. Arid Land.* **10**, 686–700 (2018).

49. IEA, "Global Energy Review 2020" (Paris, 2020); www.iea.org/reports/global-energy-review-2020.

50. J. Ding, R. J. van der A, H. Eskes, B. Mijling, T. Stavrakou, J. van Geffen, P. Veefkind, NOx emissions reduction and rebound in China due to the COVID-19 crisis. 47, e2020GL089912 (2020).

51. A. P. Tsimpidi, V. A. Karydis, S. N. Pandis, Response of fine particulate matter to emission changes of oxides of nitrogen and anthropogenic volatile organic compounds in the Eastern United States. *J. Air Waste Manage. Assoc.* **58**, 1463–1473 (2008).

52. S. Aksoyoglu, G. Ciarelli, I. El-Haddad, U. Baltensperger, A. S. H. Prévôt, Secondary inorganic aerosols in Europe: Sources and the significant influence of biogenic VOC emissions, especially on ammonium nitrate. *Atmos. Chem. Phys.* **17**, 7757–7773 (2017).

53. A. G. Carlton, C. Wiedinmyer, J. H. Kroll, A review of secondary organic aerosol (SOA) formation from isoprene. *Atmos. Chem. Phys.* **9**, 4987–5005 (2009).

54. Q. Zhang, J. L. Jimenez, D. R. Worsnop, M. Canagaratna, A case study of urban particle acidity and its influence on secondary organic aerosol. 41, 3213–3219 (2007).

55. V. Shah, J. Jaeglé, J. A. Thornton, F. D. Lopez-Hilfiker, B. H. Lee, J. C. Schroder, P. Campuzano-Jost, J. L. Jimenez, H. Guo, A. P. Sullivan, R. J. Weber, J. R. Green, M. N. Fiddler, S. Bililign, T. L. Campos, M. Stell, A. J. Weinheimer, D. D. Montzka, S. S. Brown, Chemical feedbacks weaken the wintertime response of particulate sulfate and nitrate to emissions reductions over the eastern United States. *Proc. Natl. Acad. Sci. U.S.A.* **115**, 8110–8115 (2018).

56. A. Pozzer, A. P. Tsimpidi, V. A. Karydis, A. De Meij, J. Lelieveld, Impact of agricultural emission reductions on fine-particulate matter and public health. *Atmos. Chem. Phys.* **17**, 12813–12826 (2017).

57. A. P. K. Tai, L. J. Mickley, D. J. Jacob, Correlations between fine particulate matter ($PM_{2.5}$) and meteorological variables in the United States: Implications for the sensitivity of $PM_{2.5}$ to climate change. *Atmos. Environ.* **44**, 3976–3984 (2010).

58. Z. Chen, D. Chen, C. Zhao, M. Kwan, J. Cai, Y. Zhuang, B. Zhao, X. Wang, B. Chen, J. Yang, R. Li, B. He, B. Gao, K. Wang, B. Xu, Influence of meteorological conditions on PM2.5 concentrations across China: A review of methodology and mechanism. *Environ. Int.* **139**, 105558 (2020).

59. D. M. Westervelt, L. W. Horowitz, V. Naik, A. P. K. Tai, A. M. Fiore, D. L. Mauzerall, Quantifying PM2.5-meteorology sensitivities in a global climate model. *Atmos. Environ.* **142**, 43–56 (2016).

60. J. Lelieveld, J. S. Evans, M. Fnais, D. Giannadaki, A. Pozzer, The contribution of outdoor air pollution sources to premature mortality on a global scale. *Nature* **525**, 367–371 (2015).

61. R. A. Silva, Z. Adelman, M. M. Fry, J. J. West, The impact of individual anthropogenic emissions sectors on the global burden of human mortality due to ambient air pollution. *Environ. Health Perspect.* **124**, 1776–1784 (2016).

62. C. L. Weagle, G. Snider, C. Li, A. van Donkelaar, S. Philip, P. Bissonnette, J. Burke, J. Jackson, R. Latimer, E. Stone, I. Abboud, C. Akoshile, N. X. Anh, J. R. Brook, A. Cohen, J. Dong, M. D. Gibson, D. Griffith, K. B. He, B. N. Holben, R. Kahn, C. A. Keller, J. S. Kim, N. Lagrosas, P. Lestari, Y. L. Khian, Y. Liu, E. A. Marais, J. V. Martins, A. Misra, U. Muliane, R. Pratiwi, E. J. Quel, A. Salam, L. Segev, S. N. Tripathi, C. Wang, Q. Zhang, M. Brauer, Y. Rudich, R. V. Martin, Global sources of fine particulate matter: Interpretation of $PM_{2.5}$ chemical composition observed by SPARTAN using a global chemical transport model. *Environ. Sci. Technol.* **52**, 11670–11681 (2018).

63. J. Wang, Q. Wu, J. Liu, H. Yang, M. Yin, S. Chen, P. Guo, J. Ren, X. Luo, W. Linghu, Q. Huang, Vehicle emission and atmospheric pollution in China: Problems, progress, and prospects. *PeerJ* **7**, e6932 (2019).

64. P. Thunis, B. Degraeuwe, E. Pisoni, M. Trombetti, E. Peduzzi, C. A. Belis, J. Wilson, A. Clappier, E. Vignati, PM2.5 source allocation in European cities: A SHERPA modelling study. *Atmos. Environ.* **187**, 93–106 (2018).

65. U.S. EPA, "Smog, soot, and other air pollution from transportation"; www.epa.gov/transportation-air-pollution-and-climate-change/smog-soot-and-local-air-pollution.

66. I. C. Dedoussi, S. R. H. Barrett, Air pollution and early deaths in the United States. Part II: Attribution of $PM_{2.5}$ exposure to emissions species, time, location and sector. *Atmos. Environ.* **99**, 610–617 (2014).

67. I. Bey, D. J. Jacob, R. M. Yantosca, J. A. Logan, B. D. Field, A. M. Fiore, Q. Li, H. Y. Liu, L. J. Mickley, M. G. Schultz, Global modeling of tropospheric chemistry with assimilated meteorology: Model description and evaluation. *J. Geophys. Res.* **106**, 23073–23095 (2001).

68. R. Gelaro, W. McCarty, M. J. Suárez, R. Todling, A. Molod, L. Takacs, C. A. Randles, A. Darmenov, M. G. Bosilovich, R. Reichle, K. Wargan, L. Coy, R. Cullather, C. Draper, S. Akella, V. Buchard, A. Conaty, A. M. da Silva, W. Gu, G.-K. Kim, R. Koster, R. Lucchesi, D. Merkova, J. E. Nielsen, G. Partyka, S. Pawson, W. Putman, M. Rienecker, S. D. Schubert, M. Sienkiewicz, B. Zhao, R. Gelaro, W. McCarty, M. J. Suárez, R. Todling, A. Molod,

L. Takacs, C. A. Randles, A. Darmenov, M. G. Bosilovich, R. Reichle, K. Wargan, L. Coy, R. Cullather, C. Draper, S. Akella, V. Buchard, A. Conaty, A. M. da Silva, W. Gu, G.-K. Kim, R. Koster, R. Lucchesi, D. Merkova, J. E. Nielsen, G. Partyka, S. Pawson, W. Putman, M. Rienecker, S. D. Schubert, M. Sienkiewicz, B. Zhao, The modern-era retrospective analysis for research and applications, version 2 (MERRA-2). *J. Clim.* **30**, 5419–5454 (2017).

69. K. R. Travis, D. J. Jacob, J. A. Fisher, P. S. Kim, E. A. Marais, L. Zhu, K. Yu, C. C. Miller, R. M. Yantosca, M. P. Sulprizio, A. M. Thompson, P. O. Wennberg, J. D. Crounse, J. M. St. Clair, R. C. Cohen, J. L. Laughner, J. E. Dibb, S. R. Hall, K. Ullmann, G. M. Wolfe, I. B. Pollack, J. Peischl, J. A. Neuman, X. Zhou, Why do models overestimate surface ozone in the Southeast United States? *Atmos. Chem. Phys.* **16**, 13561–13577 (2016).

70. M. Li, Q. Zhang, J. Kurokawa, J.-H. Woo, K. He, Z. Lu, T. Ohara, Y. Song, D. G. Streets, G. R. Carmichael, Y. Cheng, C. Hong, H. Huo, X. Jiang, S. Kang, F. Liu, H. Su, B. Zheng, MIX: A mosaic Asian anthropogenic emission inventory under the international collaboration framework of the MICS-Asia and HTAP. *Atmos. Chem. Phys.* **17**, 935–963 (2017).

71. J. Tollefson, How the coronavirus pandemic slashed carbon emissions—In five graphs. *Nature* **582**, 158–159 (2020).

72. S. Cicala, S. Holland, E. Mansur, N. Muller, A. Yates, *Expected Health Effects of Reduced Air Pollution from COVID-19 Social Distancing* (National Bureau of Economic Research, 2020); http://www.nber.org/papers/w27135.

73. B. N. Holben, T. F. Eck, I. Slutsker, D. Tanré, J. P. Buis, A. Setzer, E. Vermote, J. A. Reagan, Y. J. Kaufman, T. Nakajima, F. Lavenu, I. Jankowiak, A. Smirnov, AERONET—A federated instrument network and data archive for aerosol characterization. *Remote Sens. Environ.* **66**, 1–16 (1998).

74. A. Van Donkelaar, R. V. Martin, R. J. Park, Estimating ground-level $PM_{2.5}$ using aerosol optical depth determined from satellite remote sensing. *J. Geophys. Res.* **111**, D21201 (2006).

75. A. E. Christiansen, A. G. Carlton, B. H. Henderson, Differences in fine particle chemical composition on clear and cloudy days. *Atmos. Chem. Phys.* **20**, 11607–11624 (2020).

76. CIESIN (Center for International Earth Science Information Network), Gridded Population of the World Version 4 (2017), pp. 1–21.

**Citation:** M. S. Hammer, A. van Donkelaar, R. V. Martin, E. E. McDuffie, A. Lyapustin, A. M. Sayer, N. C. Hsu, R. C. Levy, M. J. Garay, O. V. Kalashnikova, R. A. Kahn, Effects of COVID-19 lockdowns on fine particulate matter concentrations. *Sci. Adv.* **7**, eabg7670 (2021).